

# We are IntechOpen, the world's leading publisher of Open Access books Built by scientists, for scientists

6,900

Open access books available

185,000

International authors and editors

200M

Downloads

Our authors are among the

154

Countries delivered to

TOP 1%

most cited scientists

12.2%

Contributors from top 500 universities



WEB OF SCIENCE™

Selection of our books indexed in the Book Citation Index  
in Web of Science™ Core Collection (BKCI)

Interested in publishing with us?  
Contact [book.department@intechopen.com](mailto:book.department@intechopen.com)

Numbers displayed above are based on latest data collected.  
For more information visit [www.intechopen.com](http://www.intechopen.com)



---

# **Oxide Ceramic Functional Thin Layer Processing by Thermal and Laser Sintering of Green Layers**

---

Guido Falk, Katrin Klein and Christoph Rivinius

Additional information is available at the end of the chapter

<http://dx.doi.org/10.5772/53257>

---

## **1. Introduction**

The growing scientific and technological significance of ceramic thin layer processing methodologies is not only due to steady growth of protection coatings against corrosion, friction and wear. By entering the micro-scale, the subject of tailoring functional interfaces raises many new questions, which are connected with an improvement of topological and microstructural characteristics of thin ceramic single layers, double layers as well as multilayers for advanced applications such as electrochemical energy storage and conversion. In this way the global importance of efficient and functional ceramic thin layers has already been recognized.

Ceramic thin film processing methodologies were also asked to be sustainable and environmentally compatible. The focus of this book chapter is therefore on laser and thermal processing of ceramic thin films from aqueous suspensions. The ceramic thin film systems assigned to the application areas of anti-wear and electrochemical functional coatings are displayed in relationship to the desired microstructural, morphological as well as compositional characteristics. In particular, the study covers comparative research results on laser sintering of dip coated substrates as well as thermal processing of electrophoretically deposited ceramic thin films. In both cases colloidal dispersed particles suspended in aqueous solutions serve as starting levels.

Particle-based processing of ceramic thin films has already been proposed for a wide range of applications. The singular advantage of this processing methodology involves the abandonment of any vacuum or inert gas conditions. Furthermore, the relatively low temperatures used result in a simple processing scheme to create complex oxide and non-oxide structural and functional ceramic coatings.

From the point of view of colloidal process engineering of structural and functional ceramics this chapter gives an overview of the technological feasibility and the potential of applications of laser and thermal ceramic thin films made from aqueous suspensions.

We consider the two applications segments of anti-wear and electrochemical functional coatings with the strongest potential to be the unique characteristics of the as-processed layered systems. Interested readers may find, both, further information about the state-of-the-art of the topic considered as well as information on future development trends.

As efficient and sustainable production technologies of ceramic thin films involve new problem solving strategies, it would be a great success for the co-authors when the reader could be motivated and activated to maximize all efforts in pursuing new avenues in the challenging research field of ceramic thin processing.

In this connection we would like to thank Rolf Clasen for his ever-lasting encouraging support and his pioneering visions that are closely connected with this displayed study. The co-authors also express their gratitude to the numerous colleagues of the institute for their effort, in particular to Christian Oswald and Doris Ranker, because, without their support the project would not have succeeded.

### 1.1. Structural ceramic thin films for anti-wear and anti-corrosion applications

Tasks of ceramic coatings are very diversified. It is expected that they protect metals from oxidation or corrosion, erosion wear, as well as thermal and electric insulation. According to the application one or more functions of the coatings stand in the forefront. The oldest process is enameling by which glass melts are deposited on a metal substrate [1, 2]. The enameling mixture, also referred to as frit, contains a high portion of oxides, specifically  $\text{SiO}_2$ . The production is made mostly on powder metallurgical processing. Metal substrates are coated by dipping or spraying, and then the enamels are melted within the temperature range between 700 °C and 900 °C.

High temperature enamels for special applications include additives of  $\text{Cr}_2\text{O}_3$ , Al, Si,  $\text{Si}_3\text{N}_4$ , SiAlON or AlN, which allow application temperatures up to 1000 °C [3]. When conventional porcelain enamels are used, the basic enamel composition contains CoO or NiO, which ensure improved adhesion onto steel surfaces as a result of interface roughening by selective corrosion. In practice cracks and spallings (fish scales defect) can occur resulting from a recombination of hydrogen diffusing from the steel interface. High temperature coatings can be produced by thermal spray process [4-7]. In this case powdered coating materials (usually granulated ceramics, agglomerate size about 30  $\mu\text{m}$  – 100  $\mu\text{m}$ ), partly or wholly melted, are deposited with high speed onto adequate substrates.

The bond to the substrate is usually determined by the mechanical interlocking of the sprayed layer. In individual cases chemical reactions can contribute to the adhesion. We distinguish between flame spraying (use of fuel gases) and plasma spraying (use of partly ionized gases within an arc). In the latter case high melt-point materials can be melted due to much higher temperature in the range of about up to 30.000 K. Complex ceramic composites, such as TiC-TiN-MoSi<sub>2</sub>-Cr<sub>3</sub>C<sub>2</sub> or Al<sub>2</sub>O<sub>3</sub> or ZrO<sub>2</sub> can be applied as substrate materials.

Meanwhile, even monolithic ceramic components can be processed by thermal spray process and higher dimensions (< 1 m) have already been realized due to the near-net shaping

character of this processing method [8]. In this case the deposition of material is applied layer by layer onto a cooled preform.

Furthermore, ceramic coatings can be processed by physical (PVD) or chemical (CVD) vapor deposition methods. Here, thermal loading of substrates is reduced compared to other coating processes [9, 10]. PVD is used to be the collective name for reactive evaporation (ion plating), sputtering, and arc discharge atomization with subsequent deposition by glow discharge. Here, also several target materials can serve as material suppliers simultaneously.

Dense hard coatings can be processed by PVD from temperatures of 300 °C. For example, columnar structured PVD-coatings are mainly processed for use in thermal insulation of highly loaded turbines.

For the CVD process, one or more reactants are chemically converted in gas atmospheres and are deposited onto a substrate in the temperature range between 600 °C and 1000 °C. The term chemical vapor infiltration (CVI) refers to the internal coating of porous preforms. Well-known examples are CVD/CVI synthesis of SiC from  $\text{SiCl}_4/\text{CH}_4$  or  $\text{CH}_3\text{SiCl}_3$ , being used for example for the processing of large-scale high-temperature SiC matrix fiber composites or for CVD-coatings of diamond-like carbon (DLC) [11].

In a few special cases sol-gel process can be used for coating of metal substrates. In this case the coatings are characterized by complex chemical composition, such as ceramic high temperature superconductors.

## **1.2. Functional ceramic thin film processing in energy materials applications**

The processing of thin ceramic layers for advanced energy storage and conversion succeeds for example with a vacuum slip casting process (VSC) [12, 13]. Disadvantages of the VSC process (such as geometrical confinement, coating quality depending on substrate characteristics) involve the development of alternative procedures, suitable for processing of advanced ceramic electrolyte layers, such as for solid oxide fuel cell (SOFC) applications. Special consideration is given to the cost factor of the processing methodologies used, as soon as large-scale production is implemented.

For the case of the tubular SOFC concept of Siemens-Westinghouse, the processing of the functional SOFC layers is therefore realized by electrochemical vapor deposition (EVD). Here, in a first step, salts are evaporated, which then react onto the substrate to the desired product under adequate boundary conditions (reactants such as oxygen or water). The pores of the substrate are closed. The further growth of the layer is determined by the (electrochemical) oxygen transport of the first layer [14-16]. This process is technically complex and not economical for a desired mass-production of SOFC systems.

The processing of SOFC electrolyte layers by laser-assisted PVD (physical vapor deposition) is subject of current research and scientific discussions. Here, a target material chemically composed of the electrolyte stoichiometry is evaporated by laser energy. The vapor is deposited onto the SOFC substrate as electrolyte layer [17].

The achieved coated surface area is currently fairly low (e.g.  $10 \times 10 \text{ mm}^2$ ). The equipment requirement with its associated costs is relatively high due to the necessary heating of the substrate and the required multiple coating processes when gas-tight coatings should be achieved.

Increased equipment investment are required for plasma spray process too [18, 19]. Furthermore, the as-processed coatings are relatively thick and porous.

Processing of SOFC coatings from liquid phases succeeds by spray pyrolysis. Here, a precursor is sprayed onto a heated substrate. Evaporation of solvent and reaction of remaining salt result in desired phase formation. Layer thicknesses of up to  $30 \text{ }\mu\text{m}$  can be achieved by a multi-layer spray pyrolysis processing [20, 21].

Wet powder spraying is a simple, easy to automate process for production of porous SOFC-cathode layers [22-24]. Layer thicknesses of up to  $50 \text{ }\mu\text{m}$  and more have already been realized on substrates of almost any size. The liquid precursor is sprayed by a spray gun. The processing of the cathode layer onto a substrate sized  $300 \times 300 \text{ mm}^2$  is usually executed within 5 minutes. Largely independent of the substrate geometry the motion unit of the spray gun (x-y-positioning system) is controlled by a central computer.

Another process for ceramic thin layer production often reported and discussed in literature is electrophoretic deposition (EPD) [25-28]. In this case the liquid suspension used is exposed to an externally applied electric field. Colloidal stabilized and charged particles move in direction to the oppositely charged electrode or a membrane, where they are collected and form a layer. Coatings of thicknesses up to several millimeters have already been realized depending on the deposition time. This fast deposition process is specifically adequate for deposition of nano-sized particles since the deposition kinetic is not dependent on the particle size.

Advanced EPD processes are based on aqueous suspensions exclusively, other EPD process methodologies use organic solvents such as acetic acid, acetone, acetyl-acetone and ethanol [29, 30].

### 1.3. Sintering of ceramic thin films

A fundamental understanding of ceramic thin film sintering on rigid substrates including a comprehensive theoretical model for the phenomenological assessment of shear and densification characteristics is given in the literature [31, 32]. A comparative study reports the resulted sintering stress calculations on the condition that the assumptions of linear viscous material behaviour and a rigid substrate material are fully respected [33]. In the event that the thin layer should not be deformable during the sintering process and any dimensional change should be completely restricted (constrained sintering) the sintering stresses as well as the strain rate can be calculated with this model too.

Other theoretical calculations comprise the sliding of the thin layer on the substrate when an equivalent friction coefficient for the interface is assumed [34-36]. This coefficient depends on the film thickness and the characteristics of the substrate.



Provided that constrained sintering conditions are fulfilled, viscous Poisson's ratio for LTCC tapes can be determined. The change of particle geometry subjected to constrained sintering conditions has already been modeled at the micro-scale. Parameters such as dihedral angle, grain size of the particles, thin film densification rate as well as surface and grain boundary energy are taken account in the model [37, 38]. The described reproduces the equilibrium shape of the initially spherical particles during the thin film densification process. The distance between the centers of gravity of the particles is assumed to be constant.

Another approach is based on a Monte Carlo study in order to solve the viscous flow problem during densification process of thin layers [39]. Based on this work numerical simulations have been elaborated [40, 41]. Close to free edges, sintering density is inconsistent after sintering process and deformation of the sintered geometry is observed. In the immediate vicinity of the free edge the density is uniform, however. This free edge mechanism is particularly critical as soon as the dimension of the sintered structure is reduced and the thickness is not negligible in comparison to the lateral dimension. However, the accuracy and applicability of the simulated densification behaviour of constrained sintered layers should always be put into relation with experimental data and observed findings.

If conditions of constrained sintering are met significant sintering stresses will appear within thin layers that result in reduced densification rates [42, 43]. Additionally, in the specific case of sintering thick layers the constrained sintering condition is only applied alongside surfaces of the sintered body. By that way, the free surfaces such pores within the sintered layer are not perfectly constrained resulting in a curvature and distortion of surficial areas.

Tensile stresses that reduces driving sintering forces have already been modeled by Finite Element Analysis (FEA) [42]. In the exemplary case of  $\text{Al}_2\text{O}_3$ /glass-interfaces it was shown that these tensile stresses decrease in through-thickness direction towards the middle of the interface as well as in close vicinity to free edges. These simulations have been verified by experimental data and showed good correlation between modeled and experimental data.

Owing to the option of applying significant quantities of targeted heat into surficial layers of a material by laser energy, laser processing methodologies are well suited to sintering of particulate thin films coatings. Thus one can coat ceramic substrates with metal layers as well as ceramic coatings on metal substrates. From a technological point of view the latter case is easier to implement. For example, ferrite powder is easily sintered onto PZT (lead zirconate titanate) substrates by laser energy [44]. The advanced densification of ceramic coatings and thin films on metal substrates by laser energy is more sophisticated. Here, care must be taken to ensure that the interfacial temperature between the layer and the substrate does not exceed the melting temperature of the supporting material. When precise process engineering is guaranteed then sintering of a ceramic protection layer, for example yttrium stabilized zirconia (YSZ) and alumina ( $\text{Al}_2\text{O}_3$ ) on high-temperature steel substrates is possible.

However it must be noted that the laser sintering process must be subjected to the prior powder accumulation and pre-sintering in order to keep the exposed overall surficial laser energy as low as possible [45]. However, the use of sinter active powders will facilitate the

laser sintering process and might lead to the bypassing of complex powder accumulation and pre-sintering processing steps.

For example, electrophoretically deposited alumina green layers have already been laser sintered on standard chromium and chromium-nickel steels, though under inert gas atmosphere conditions [46]. Moreover, laser sintering of powdered YSZ green layers on TiAl6V4-alloy substrates has already been reported [47].

## 2. Advanced deposition of oxide ceramic thin films from aqueous solutions

### 2.1. Electrophoretic deposition of tubular ceramic thin films

Electrophoretic deposition of nano and sub-micron sized particles represents a technologically attractive and relatively simple method. The shaping of homogeneous 2D and 3D green bodies is achieved during the deposition process (electrophoretic transport and electroosmotic interfacial kinetics) without the need of additional operating steps [48]. Further advantages compared with other procedures are shortest possible process times and the simple design of the deposition equipment. The EPD process consists of two sub-processes. The charged particles are attracted first to the electrode or interface of the opposite polarity (electrophoretic transport) under the influence of an external electric field. In a second step, particles are deposited onto the polar substrate under the influence of interfacial electrohydrodynamic kinetics (electroosmosis of the second kind). Since the deposition rate is independent of the particle size, the EPD methodology is specifically suitable for shaping of complex green bodies made of nano-sized particles. Especially in this case, green densities achieved are significantly higher compared to other shaping methods [49]. Furthermore, processed green bodies exhibit excellent homogeneities of particle packing [50]. Within the following investigations the EPD processed green thin film layers are exclusively produced from aqueous suspensions. The substrates are micro-tubular pre-sintered NiO-YSZ composites processed by powder injection molding (PIM). The experimental EPD-setup is represented in the following Figure 1. The polarizable NiO-YSZ substrate is fixed to the centered support by means of a clamp mechanism and is stabilized by a central Pt-wire ( $\xi$  0.5  $\mu\text{m}$ ) working as anode. At the same time the NiO-YSZ substrate subdivides the setup into two chambers. Inside the micro-tubular substrate there is the compensation chamber housing the electrolyte solution. The suspension chamber is arranged between the outer tubular shaped cathode made of graphite and the micro-tubular NiO-YSZ support.

The electrical conductivity of the electrolyte solution is 10-fold higher than the electrical conductivity of the aqueous suspension. The inside diameter of the EPD cell amounts 15 mm, with a height of 70 mm.

As the parallel processing of green thin film layers enables higher throughput, another experimental EPD setup has been realized, as it is shown in Figure 2. Thereby, seven micro-tubular substrates can now be coated simultaneously.

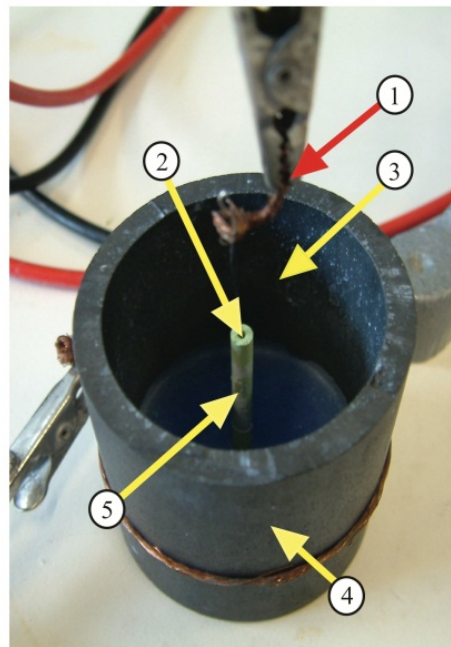


**Figure 1.** Experimental setup of the membrane type EPD cell arrangement. The negatively charged YSZ particles of the suspension are deposited onto the outer surface of the porous Ni-YSZ micro-tube (1: anode; 2: compensation chamber; 3: suspension chamber; 4: cathode; 5: Ni-YSZ micro-tube).

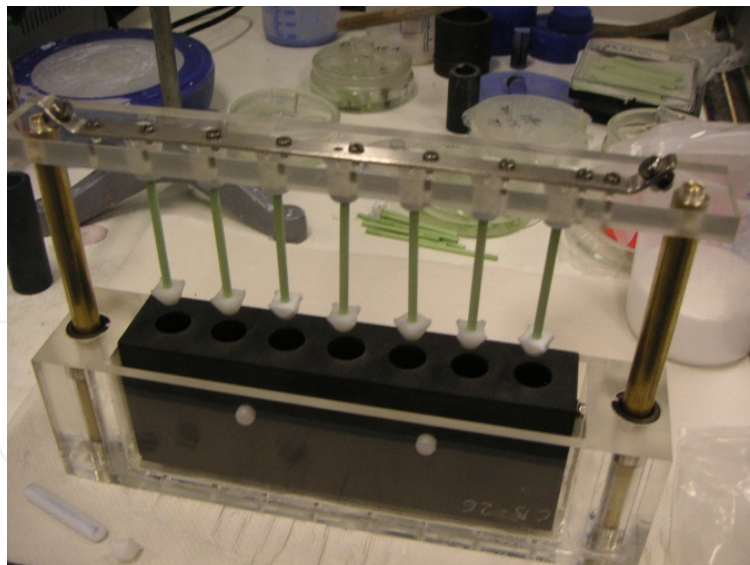


**Figure 2.** Experimental multi-cell EPD setup for the simultaneous EPD-coating of seven micro-tubular cells.

Even in this case, the Pt-wire anode is characterized by a diameter of 0.5 mm. The cathode also consists of a graphite block CB26 (Carbon Industrie-Produkte GmbH, Germany) (dimensions: 185.5 mm wide, 67 mm deep, and 36 mm thick). Seven center-holes in the block of 15 mm in diameter are arranged. The experimental setup enables a reduction of the dead



volume in the deposition cell, so contributing to reducing waste suspension. In order to avoid that graphite particles become detached, the graphite block was flushed with cleaning solutions and cleaned in an ultrasonic unit. Holders and rails are made of POM (polyoxymethylene) with sealing made of duplicating silicone. Various centering gauges made of POM, Teflon and POM/duplicating silicone combinations have been tested. In Figure 3 the brackets for the micro-tubular substrates is displayed. Compared to the single-cell EPD setup this multi-cell setup the compensation chamber is not perfectly sealed off from the suspension chamber. By that way, the suspension is taking over the function of the electrically conductive electrolyte too.

The micro-tubular substrates to be coated are soaked in an electrolyte solution of 20-fold increased electrical conductivity in relation to the suspension. Subsequently, the micro-tubular substrates are positioned on the Pt-electrode wire and the centering gauges are put in place at the pipe endings.

The Pt-wire threaded micro-tubes are lowered down into the suspension and the voltage is applied. After switching off the electric field, the rails are removed from the suspension chamber and the coated micro-tubes are mounted in a frame and stored for drying.

The following Figure 3 displays the EPD coated micro-tubular substrates immediately after the deposition process.

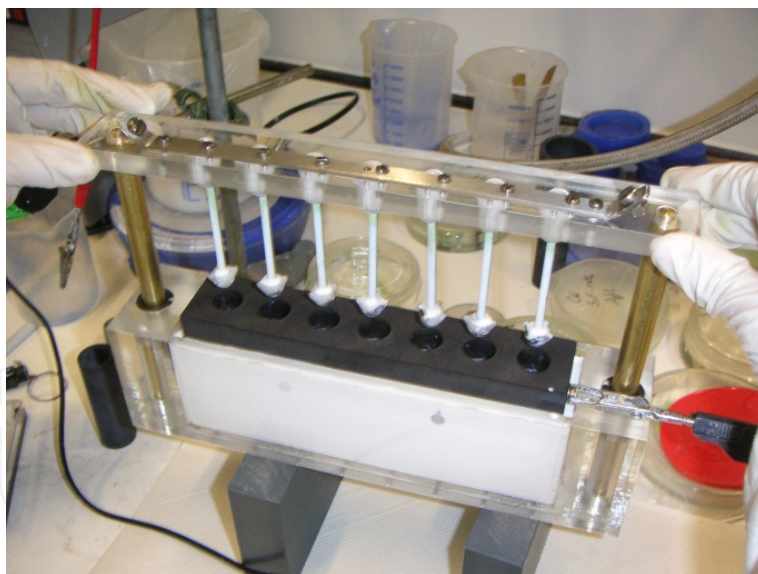


**Figure 3.** YSZ-coated NiO-YSZ micro-tubular substrates immediately after processing by the multiple-cell EPD deposition setup.

## 2.2. Dip coating

According to the dip coating procedure described herein  $\text{Al}_2\text{O}_3$  thin films are processed onto borosilicate glass flat specimen. Suspensions used have been prepared by aqueous colloidal processing route. Hanging on the rails the substrates become immersed in the suspension and

are retracted after a short deposition period. The parameters such as feed speed, plunge speed, holding time, and drawing speed are controlled automatically by a remote control system.

Start and end points of the immersion process are freely selectable and are only limited by the dimensions of the experimental setup.

By that way it is possible to coat various-sized substrates with the same settings. Pilot trial experiments designed to test rheological characteristics of the suspensions have been made on soda lime glass substrates. Laser sintering experiments were conducted with borosilicate substrates later on with the same proven parameters again. The following Figure 4 depicts the experimental dip coating setup used.

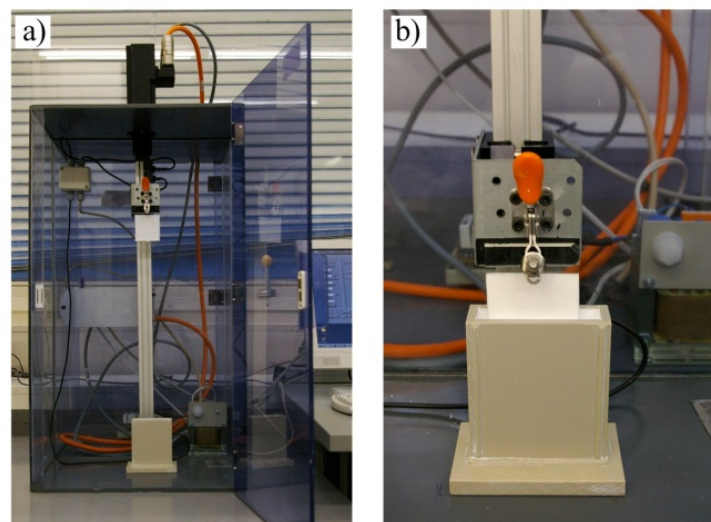


**Figure 4.** Experimental setup of the remote controlled dip coating setup (a) and removal of a borosilicate substrate during the dip-coating process (b).

In dip-coating technology, the properties of gelatine forming additives in terms of film formation, thermoreversibility and adhesion are particularly important. Therefore, the use of preheated substrates within the temperature range between 80 °C and 100 °C have been investigated. This processing option is hereinafter referred to as “thermogelation”.

The coated substrates are hung on a specific sample holder and dried for 24 hours under ambient laboratory conditions after being pulled out of the dipping chamber. The dip-coating drawing speed was varied within a certain experimental matrix in order to determine the optimum thin layer characteristics suitable for laser sintering. The remote controlled drawing speeds used were within the designated interval of 8.33 mm/s to 33.3 mm/s.

In order to establish a correlation between dip-coating drawing speed and rheological characteristics of the suspension, it is necessary to analyze viscosity with a conventional rheometer at shear-rate conditions that are relevant for the dip-coating process. For this, the trajectory velocity on the outside of the cylindrical body has to be calculated out of the rotation speed of the cylindrical body. This calculated speed can be compared with the dip-coating drawing speed realized during the dip-coating process. The quantitative derivation of

these equations is given in the literature [51] and consequently there is a direct connection between the shear-rate and the dip-coating drawing speed.

The following Table 1 provides the dip-coating drawing speeds as well as the calculated shear-rates of the experimentally realized dip-coating conditions.

drawing speed (mm/s)	shear rate (s <sup>-1</sup> )
33.3	24.1
16.6	12.1
8.3	6.0

**Table 1.** Dip-coating drawing speeds and corresponding shear-rates realized from the dip-coating processes

3. Laser assisted surface engineering processes

3.1. Laser sintering system and components

The laser processing of the dip coated specimens is made by a prototypical CO<sub>2</sub>-laser setup constructed and designed by Fa. Auratech (Austria). The applied CO<sub>2</sub> slab laser (Rofin Sinar Ltd.) delivers an output power of 100 watts at pulse frequency of 20 kHz and an output stability of ± 7%. The wave length of the laser is 10.6 μm. The scanner unit, which is installed downstream the laser emission enables to precisely control the physical travel of the laser beam within the x- and y-direction. By that way, the user can home in on any location of an area of 100 mm x 100 mm. The laser travel speed can be controlled up to 7500 mm/s. The following Figure 5 depicts the laser equipment used for the laser sintering and densification of green ceramic thin films.



**Figure 5.** Prototypical CO<sub>2</sub>-laser sintering facility used for sintering and densification of green thin film ceramic layers.

Through the use of scanner unit and most modern machines and hardware equipment the good focussing of the laser beam allows power densities that can barely be reached by conventional weld processes. The height adjustable and heated sample changer allows the variation of the focal spot diameters in the range between 350  $\mu\text{m}$  and 7.5 mm.

The heated sample holder enables adjustable substrate temperatures up to 540  $^{\circ}\text{C}$  in order to reduce the risk of thermal stress formation during laser operation. Therefore the installed electric heating plate (Thermolyne Cimarec, Thermo Fisher Scientific Inc., USA) is characterized by thermostatic control and a protecting plate made of alumina (see Figure 6).

Since laser processing of green ceramic thin films is a function of a number of substance and device specific parameters, an adequate parameter matrix has been tested. Key parameters are focal spot diameter of the laser, and laser power. These two parameters are applied for the calculation of the power density. The travel speed of the laser,  $v_{\text{scan}}$ , is another important parameter in achieving optimum heat transfer rates. The pulse frequency was kept at a constant level of 20 kHz for all displayed results. Furthermore, the retaining speed of the scanning beam was not changed during laser operation and was set to the factory default level of 7477 mm/s.

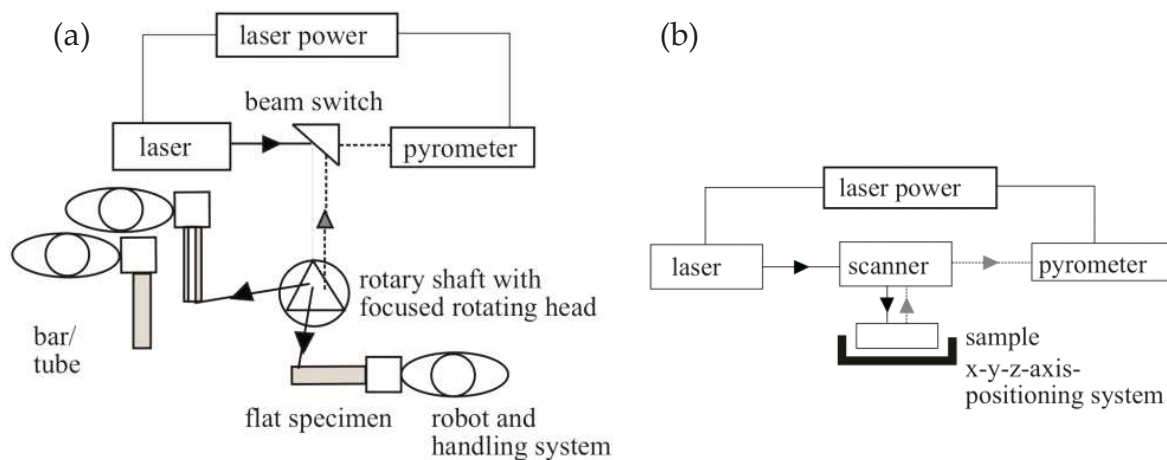


**Figure 6.** Schematic of the experimental laser sintering and densification setup with the option of defocused operation (a) and focused operation mode (b).

### 3.2. Laser sintering and laser consolidation

Processes of laser consolidation and laser sintering comprise the scanning the sample surface by a focused laser beam. The motion system is usually numerically controlled. Here, small line spacing resulting in a high overlap and energy input result in balling. As soon as the scan spacing exceeds the focal diameter the as-sintered and as-consolidated thin films become fragile.

It should also be underlined that the measured distance between two lines on the sample surface can deviate significantly from the line spacing fixed with a software programmed input mask. This is because the scanning unit shows significant aberrations such as astigmatism for



angular incident beams caused by the specific dimensions of the rotating mirrors used. Depending on the present distance between sample and focal plane of the scanning unit the real line spacing increases or decreases. These aberrations may be offset with correction files controlled by the software settings. Each correction files only correct the error at a single working plane. In order to guarantee a high flexibility during laser processing the implementation of correcting files is omitted in this study. Later in this study it distinguishes between “line spacing” conventionally set via the software and “real line spacing” at the sample surface. The following Figure 7 depicts a schematic of the varied adjustment and activation options of the scanner unit. The schematic shown in Figure 7b represents the only possibility to guarantee a homogeneous temperature distribution along the entire sample surface.

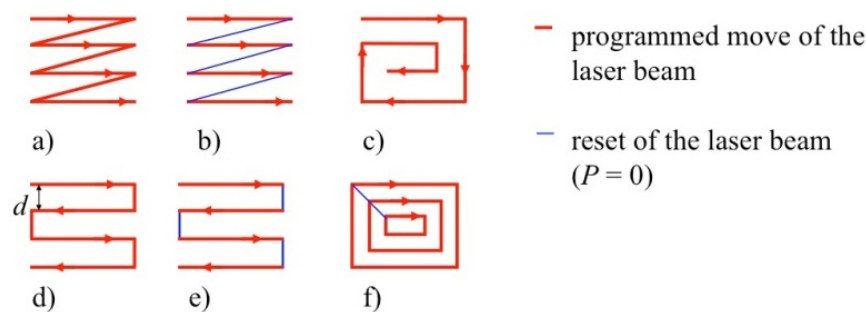


**Figure 7.** Schematic of varied adjustment and activation options of the scanner unit used for laser sintering and laser consolidation.

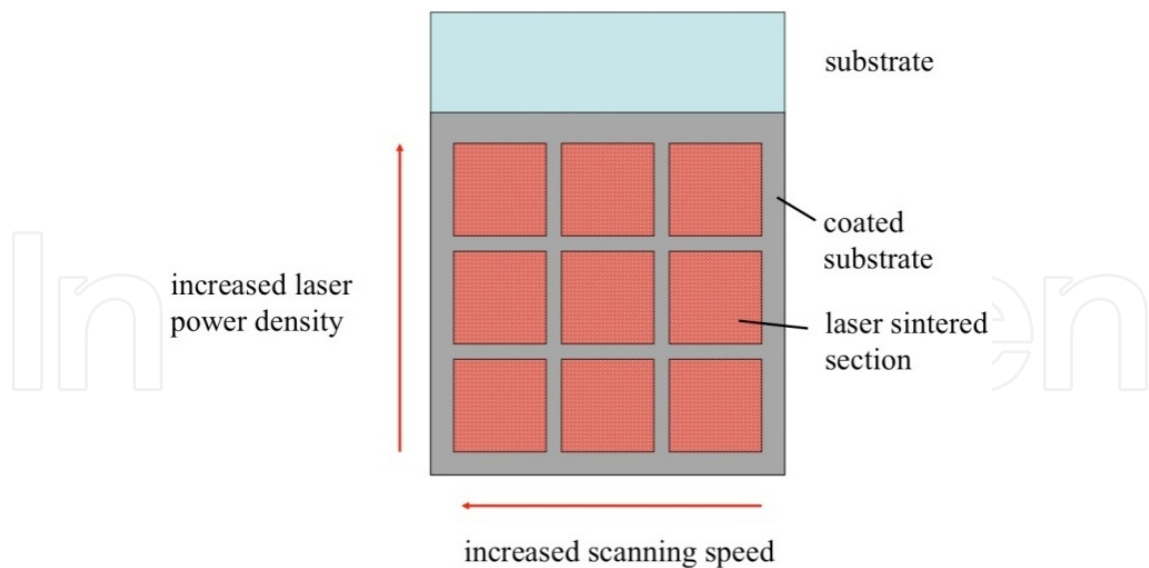


**Figure 8.** Schematic of the procedure for the determination of energy densities realized by laser irradiation of ceramic thin films made of  $\text{Al}_2\text{O}_3$  deposited onto borosilicate substrates.

The laser scanning shown in Figure 7a, 7d and 7e results in an irregular temperature distribution on the edge of the laser scanned sample surface due to the heat flow transmitted



from the irradiated surface towards the surrounding, cooled zones of the material. The scanning given in Figure 7c and 7f lead to a rise in temperature in the center of the laser irradiated sample area. The following Figure 8 depicts the procedure for the determination of the energy densities that are at least required in order to realize complete melting of the deposited thin film layer, and in this way achieving the necessary transparency.

With the laser scanning technology used the substrate is laser irradiated on nine sample segments characterized by different laser parameter combinations. In particular, the laser treated lines are irradiated at constant laser energy density and the laser treated columns are irradiated at constant laser travel speed. Not only we adapt suitable combinations of laser parameters to improve the surface characteristics of the irradiated sample surfaces, but we also use multi-laser irradiation procedures. In the latter case, the irradiated area is scanned multiple times with the same parameters. Only scanning directions are varied in this case.

### 3.3. Laser ablation

Simple line scanning experiments are performed in order to find essential basics and to understand the opportunities and limits of micro-structuring of surfaces by laser ablation. For example, enabling complex 2D and 3D geometries the scanner software used offers two options: First, specially created and designed vector graphic files can be used as template. On the other hand, any Graphic files can be imported and converted to scanner bitmaps. The conversion is necessary, because the scanner unit is not able to process gray scale pictures. Therefore, the optimal solution is to use graphic templates in duplex format, in other words, graphics that are composed exclusively from white and black pixels. JPEG and BMP-format templates usually have smoothed edges by using different gray scales (see Figure 9a). Visible artifacts appear by using such templates for converting into a scannerbitmap as it is shown in Figure 9b. The development of artifact formation also depends on the sized of the given pixels. The smaller the pixel size is, the less important is the artifact formation. The pixel size, however, is limited downward by the focal-spot: If the pixel size is smaller then the focal spot of the laser beam, there will be multiple irradiation of the surface area and in consequence to an increased material removal.

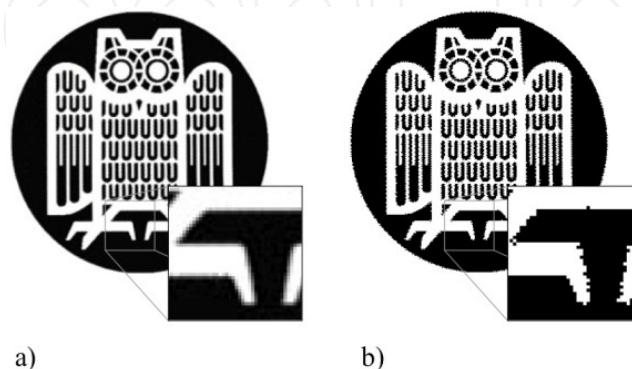


**Figure 9.** Formation of artifacts caused by the conversion of a graphic template into scanner bitmaps: template (a) and converted bitmap (b)

Laser travel speed as well as laser power will be adopted after the conversion of the template into the scanner bitmap format. However, line spacing is influenced by the pixel size. The scanning unit controls line by line the individual pixels. This process refers to the scanning with a laser travel speed  $v_{\text{scan}}$  analogous to the laser sintering process. Depending on the pre-configuration the black or white pixels are irradiated.

### 3.4. Laser micro-structuring

In addition to laser sintering, laser consolidation and laser ablation, the laser equipment depicted and described above is also suitable to process micro-structured decals used in the processing step of ceramic surface finishing. In general, three different processing routes have already been verified. First, the decals are processed by selective laser sinter (SLS) onto flat glass samples. Two alternative processes are depicted in the following Figure 10.

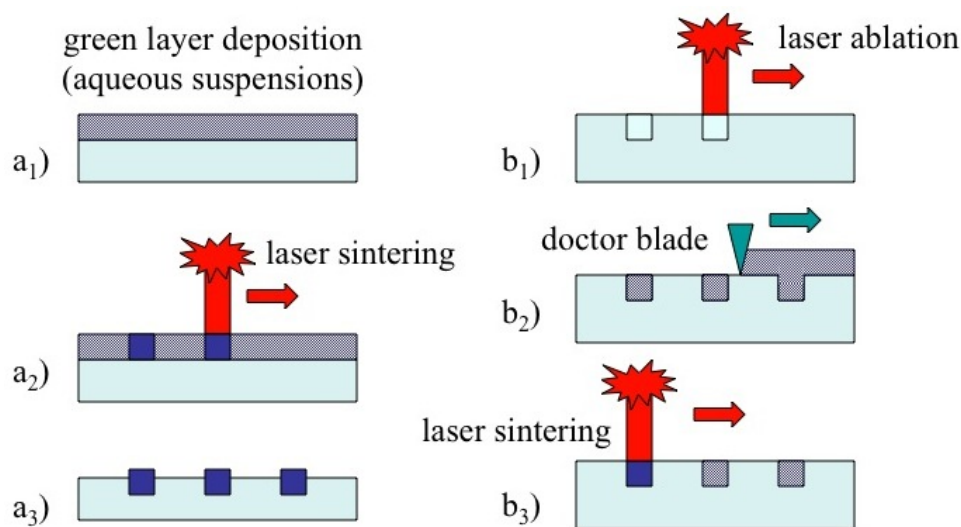


**Figure 10.** Alternative micro-structuring of glass surfaces by laser energy.

For the decal laser processing, the process depicted on left side of Figure 10, comprise the deposition of a green layer made onto the glass substrate ( $a_1$ ). Such a system can be established by means of dip-coating, spray processing or painting. Selective areas are irradiated by laser energy after drying ( $a_2$ ). By that way, the particles are intended to sink into the glass surface. After laser processing the selective irradiated surface sites remain structured by the coated powder ( $a_3$ ). The process depicted on the right side of Figure 10 represents a combination of laser ablation and laser sintering. First, pits, recesses, and anomalies are processed into the surface by means of laser ablation ( $b_1$ ). The injuries are then filled up with the dry or liquid coating material. During wiping of the excess coating material with a squeegee, it should be guaranteed that the deposition of coating material is exclusively restricted to the laser ablated surface sites. The non-treated surface remains almost free of deposited material ( $b_2$ ). The surface is irradiated by laser energy after drying and consequently, a proper bonding between the coating material and the substrate is achieved ( $b_3$ ).

## 4. Thermal processing of thin YSZ-electrolytes for SOFC applications

### 4.1. Sintering of YSZ thin films

We investigated the influence of sintering parameters on micro-structure of electrolyte and anode substrate respectively for given EPD boundary conditions: the electrical field strength was set to 30 V/cm, and the deposition was fixed to 30 seconds. PIM processed and pre-sintered NiO-YSZ substrates were characterized by mean pore diameter in the range between of 150 nm and 200 nm. The following figure 11 below depicts an example of the macrostructure of the EPD-coated micro-tubular composite after sintering at 1400 °C (heating rate 10 K/min and holding time 10 min).



**Figure 11.** YSZ coated and sintered NiO-YSZ micro-tubular substrate.

As with all thermal sintering investigation considered in this study the sintered electrolyte layers were transparent. The following Figure 12 shows an EDX-line-scan of a sample sintered at 1380 °C (heating rate 5 K/min, holding time 30 min).

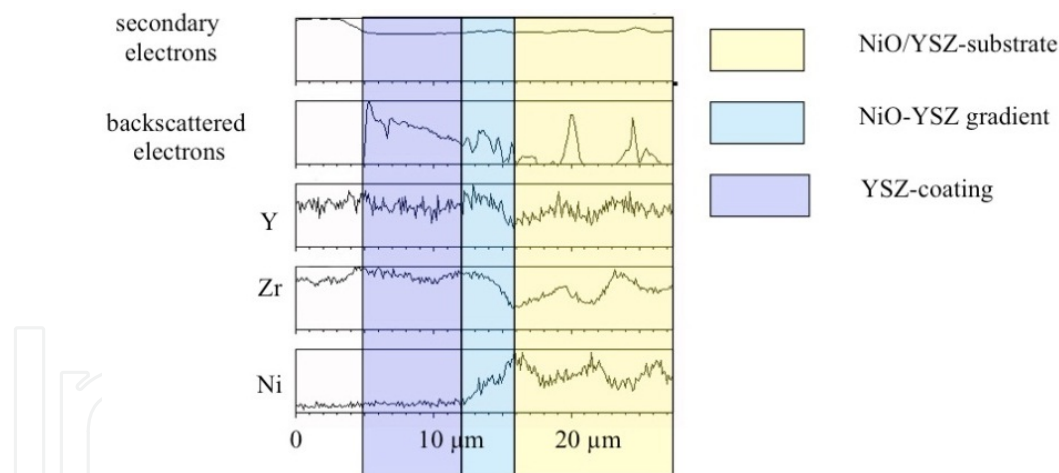


**Figure 12.** EDX-line-scan of the cross section of a YSZ coated NiO-YSZ micro-tubular substrate.

In this specific case the EPD deposition parameters were fixed to electric field strength of 20 V/cm and deposition time of 60 s. The multilayer structure of the coating composed of the anode substrate, a gradient interlayer and the electrolyte is clearly visible.

### 4.2. YSZ thin film morphology and green density correlation

In the following Figure 13 SEM topographies of green layers are compared with sintered layers thermally treated at 1400 °C (heating rate of 10 K/min, holding time 10 min). In the

light of these data and analysis results provided by the study, it may therefore be concluded that high green layer densities lead to higher grain size.

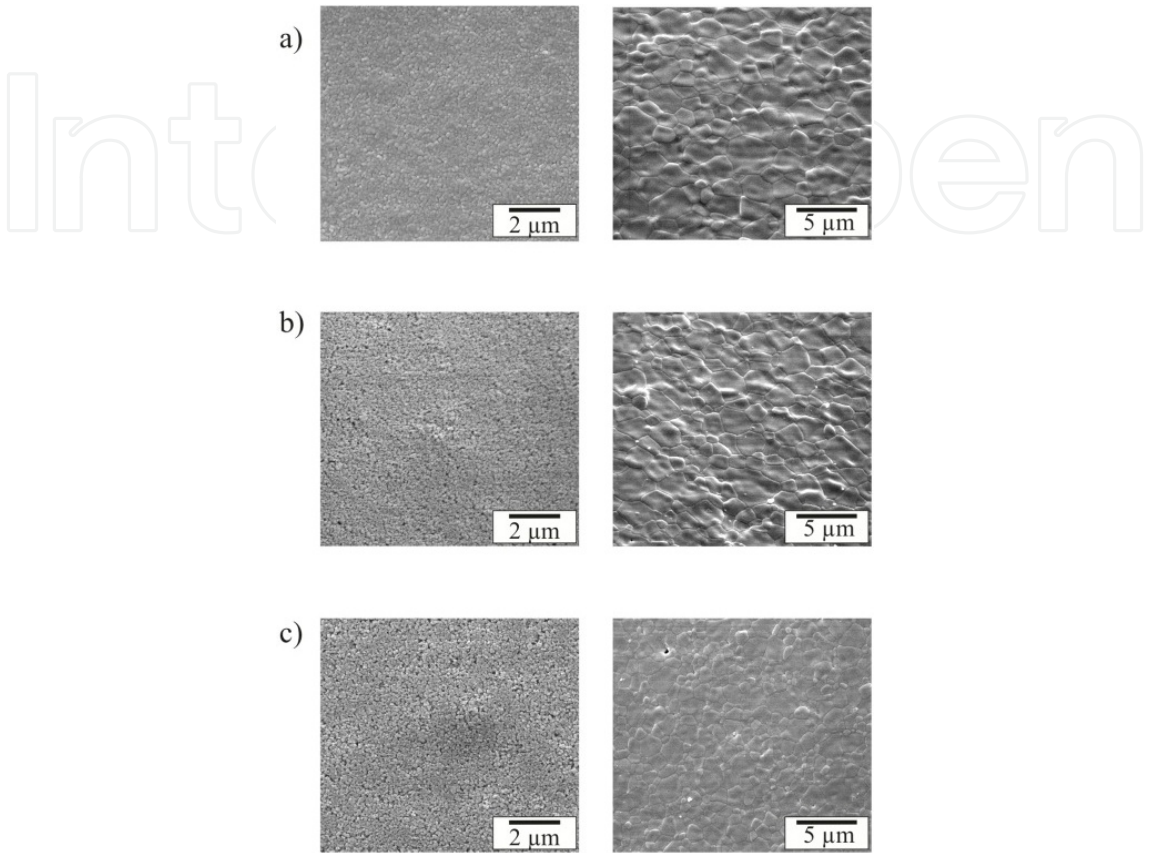


**Figure 13.** SEM topography of green electrolyte layer (left) and sintered electrolyte layer (right). Suspension and EPD characteristics are set to (a) 5 wt.-% YSZ, 3 wt.-% polyelectrolyte additive, E = 30 V/cm, t = 30 s; (b) 15 wt.-% YSZ, 1 wt.-% polyelectrolyte additive, E = 30 V/cm, t = 10 s; (c) 10 wt.-% YSZ, 0.3 wt.-% polyelectrolyte additive, E = 35 V/cm, t = 5 s.

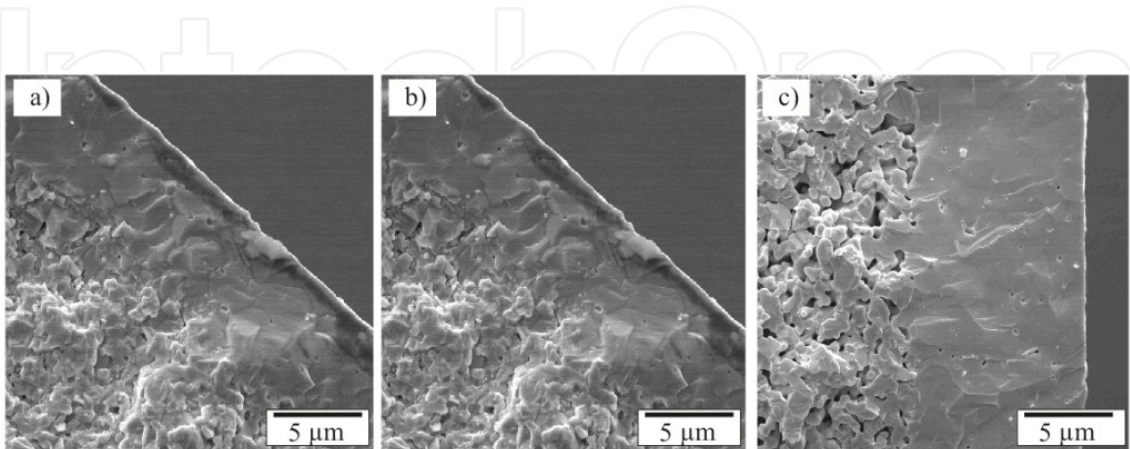


**Figure 14.** SEM topographies of breaking edges of three thermally sintered YSZ layers. The processing conditions correspond to those given in Figure 13.



SEM topographies of breaking edges of the samples shown in Figure 13 depicts that different green densities do not influence the sintering densities and the residual porosity of the electrolyte layer (see Figure 14).

#### 4.3. Two-step thermal processing of YSZ thin films

Initial steps toward consolidating the layered microstructure were implemented successfully by two-step-sintering approach in order to achieve high densification rates of the sintered electrolyte layers at reasonable mean porosity values of the anode substrate. In addition to this objective, the two-step-sintering approach intends to achieve high densification rates at relatively low grain growth rates. Thermal analytical methods, such as thermogravimetry, differential thermogravimetry and dilatometry up to 1500 °C was used, in order to compare sintering shrinkage of anode substrates between one-step sintering and two-step-sintering approach. The following Figure 15 shows the porosities of the anode substrates as well as the YSZ grain sizes achieved as a function of the thermal sintering methodology used.

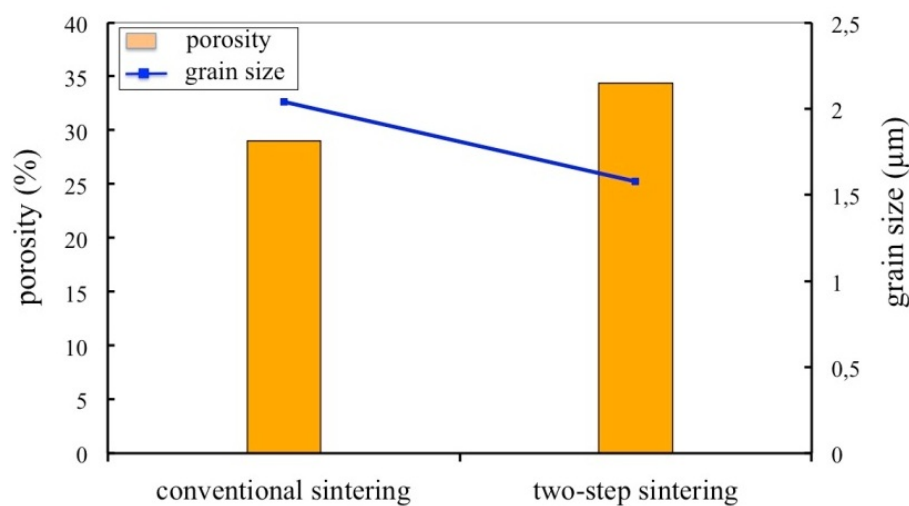


**Figure 15.** Porosities of the anode substrate and YSZ grain sizes of micro-tubular NiO-YSZ anode substrates sintered conventionally at 1400 °C (holding time 10 min) and sintered by two-step-sintering at 1300 °C (holding time 30 min) / 1200 °C (holding time 10 hrs.)

It is clearly shown that the shrinkage by two-step-sintering has been significantly reduced. According to these investigations, the conventionally sintered electrolyte layers are characterized by a mean grain size in the range of 2 μm, whereas the mean grain size of the two-step-sintered electrolyte layers is 1.6 μm. On the basis of the experimental sintering data and the analysis of the breaking edges shown in the following Figure 16, it is evident that electrolytes sintered by two-step-sintering show significantly increased densification. The better suitability of two-step-sintered electrolyte layers can easily be seen in Figure 16 b. Here, a full densification of the electrolyte thin film was only achieved during the second sintering step.



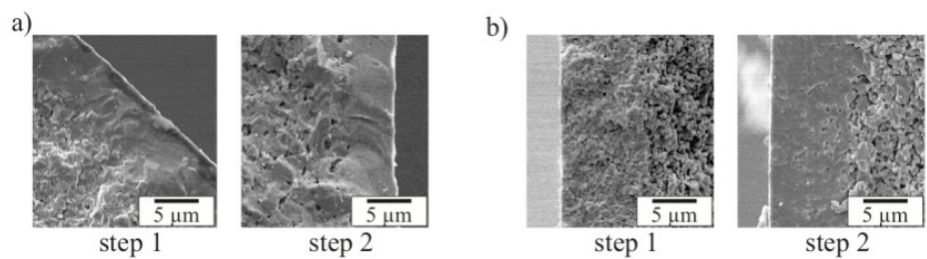


**Figure 16.** SEM topographies of breaking edges of two-step-sintered YSZ electrolyte thin films processed by EPD. (a) two-step-sintering at 1400 °C (holding time 10 min) / 1250 °C (holding time 10 hrs.) and (b) two step sintering at 1250 °C (holding time 30 min) / 1150 °C (holding time 10 hrs.).

The effects of different two-step-sintering conditions on the porosity and shrinkage behavior of the NiO-YSZ anode substrates are depicted in the following Figure 17.

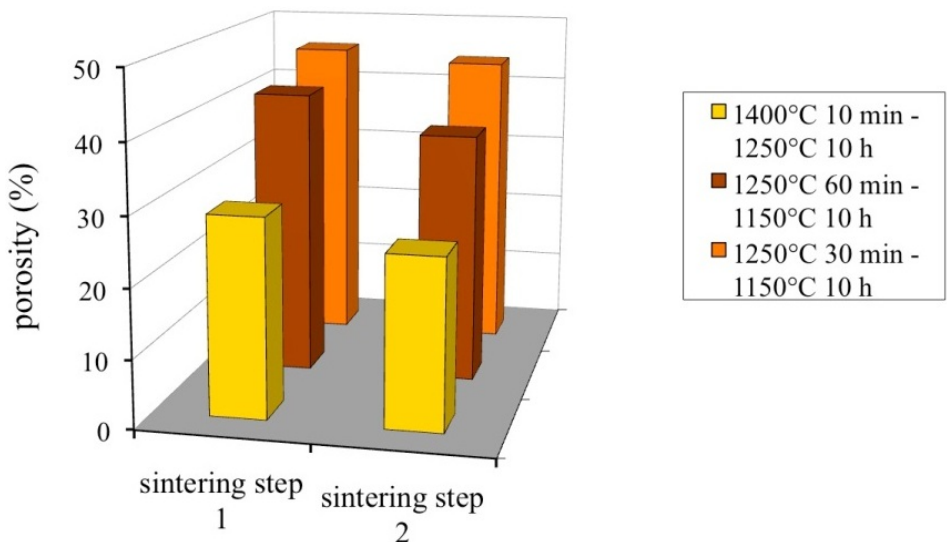


**Figure 17.** Densification behavior of NiO-YSZ substrates, two-step-sintered at different sintering conditions.

Investigations regarding the film thicknesses of the as-sintered layers revealed mean values in the range between 3.5 μm and 15.5 μm at EPD coating conditions of 30 V/cm (applied electric field) and deposition time of 30 s. Different thin film thicknesses were almost impossible to be correlated with the sintering programs used, because over the entire sample cross section the thickness variation was in the range of about 8 μm. Specific coating condition (35 V/cm at deposition time of 5 s) lead to a reduced thickness variation in the range of 3 μm.

#### 4.4. SEM/EDX characterization of YSZ thin layers

Initial tests of SOFC-systems, made of micro-tubular anode-electrolyte composites presented in this study, resulted in a performance of 1.7 W at operating temperature of 850 °C, which corresponds to a power density of 400 mW/cm<sup>2</sup>.

A prototype of the cell is shown in the following Figure 18a. Figure 18b depicts the SEM topography of the cross-sectioned structure of NiO-YSZ substrate, YSZ electrolyte layer and LSM cathode processes by wet powder spraying.



**Figure 18.** Prototype of a micro-tubular SOFC cell (a) and SEM topography of the cross-sectioned structure of NiO-YSZ-substrate, YSZ electrolyte and LSM cathode.

The following Figure 19 shows the EDX mapping of the three layer systems of NiO-YSZ anode support, YSZ electrolyte and LSM cathode. It is shown that faulty anode edges are automatically smoothed by the EPD processed YSZ layer.

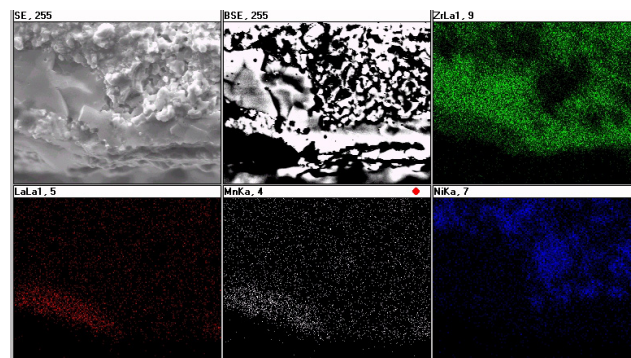


**Figure 19.** EDX mapping of the three-layer systems of NiO-YSZ anode support, YSZ electrolyte and LSM cathode. Above, from left to right: secondary electron image, back scattered electron image, Zr element distribution. Bottom, from left to right: La, Mn and Ni element distribution.

## 5. Laser processing of anti-wear resistant alumina thin layers

The laser processing investigations should take all reasonable steps to ensure that wet deposition and subsequent laser irradiation of different  $\text{Al}_2\text{O}_3$  coating specifications would result in superior wear resistance and anti-scratch behavior of coated borosilicate glass surfaces.

On these aspects  $\text{Al}_2\text{O}_3$  suspensions have been prepared according to precautionary specifications, whilst at guaranteeing optimum quality of processing.

### 5.1. Powder, substrates and substrate pretreatment

Tailor-made submicron  $\text{Al}_2\text{O}_3$ -particle suspensions doped with 10 wt.-% methylcellulose (MC) binder additives have been produced. Furthermore all suspensions have been dispersed with 2 wt.-% anti-foaming agents. The following Figure 20 shows the viscosity of three different  $\text{Al}_2\text{O}_3$  suspension qualities as a function of the shear rate.

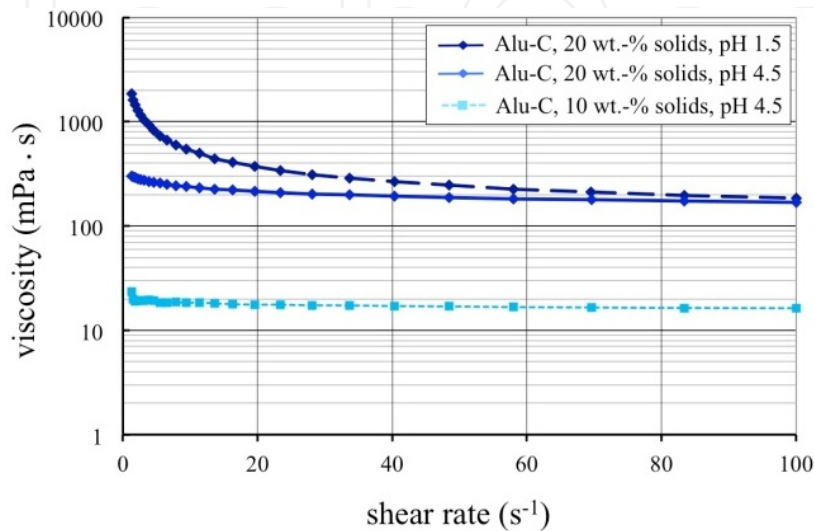


**Figure 20.** Viscosity as a function of the shear of three different  $\text{Al}_2\text{O}_3$ -suspension qualities. The variations pertain pH value and particle concentration.

Suspensions with a particle concentration of 10 wt.-% are characterized by almost Newtonian flow behavior. Due to increase of particle concentration to 20 wt.-%, a tenfold and upward increase in viscosity is even possible. Therefore, it is not possible to further increase the particle concentration of  $\text{Al}_2\text{O}_3$ -suspensions, because the resulting viscosity increase makes it impossible to use these suspensions for dip coating. Second, the lowering of the pH-value to below 1.8 to 1.5 causes significant increase of viscosity, especially at small shear rates. This impact is almost compensated for shear rates exceeding values of  $80 \text{ s}^{-1}$ . Since the relevant shear rates realized during dip-coating deposition process attain values in the range of about  $24 \text{ s}^{-1}$ , tailoring of the suspensions was performed in consideration of mean shear rate levels below of  $24 \text{ s}^{-1}$ .

### 5.2. Surface characterization

The mean diameter of agglomerates formed in the suspension must be smaller than the thickness of the processed layer, in order to realize homogeneous dip-coated layers. Figure 21 provides an overview with the best possible combination of coatings processed with different  $\text{Al}_2\text{O}_3$  powder qualities characterized by different mean particle diameters  $d_{50}$  as well as specific BET surface areas  $A_{\text{spec}}$ .

The following Figure 22 depicts the curves of the as-processed layer thicknesses as a function of the distance from the sample lower border and the different powder qualities, in order to quantify the different impact of the various processing conditions.

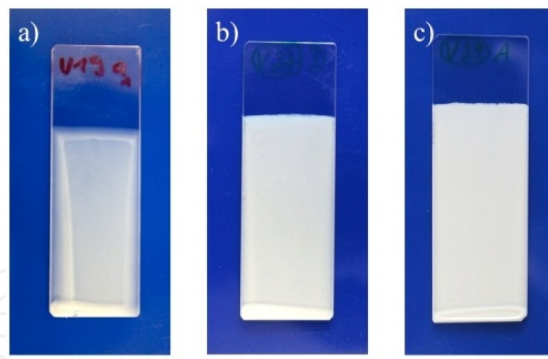


**Figure 21.** Green thin film layers processed by dip-coating onto silica glass substrates. The  $\text{Al}_2\text{O}_3$  qualities used are (a) Alu-C, Evonik Degussa, Germany,  $d_{50} = 13 \text{ nm}$ ,  $A_{\text{spec}} = 50 \text{ m}^2/\text{g}$ ; (b) AKP-50, Sumitomo Chemical Ltd., Japan,  $d_{50} = 200 \text{ nm}$ ,  $A_{\text{spec}} = 10.6 \text{ m}^2/\text{g}$ ; (c)  $\text{Al}_2\text{O}_3$  Alfa Aesar, Germany,  $d_{50} = 2.07 \mu\text{m}$ ,  $A_{\text{spec}} = 11.3 \text{ m}^2/\text{g}$ . The dip-coating was performed at a particle concentration of 30 wt.-%, a drawing speed of 33.3 mm/s and pH 4.5.

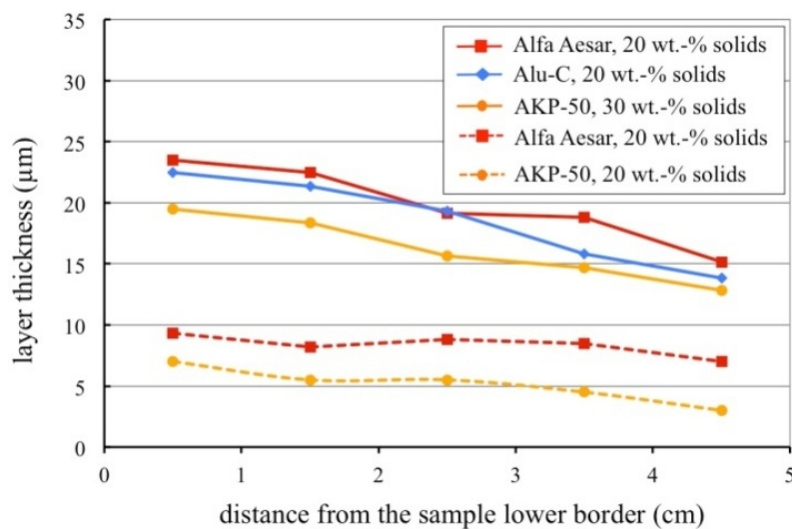


**Figure 22.** Comparison of the as-processed layer thicknesses of different dip-coated alumina layers.

This Figure shows that the largest layer thickness can be achieved using a combination of Alfa Aesar powder quality as well as a particle concentration of 30 wt.-%. Values at similar levels were determined for Alu-C suspensions with a particle concentration of 20 wt.-%. The layer thicknesses having achieved with AKP-50 suspensions with a particle concentration of 30 wt.-% were below these corresponding values mentioned above. Layers made of AKP-50 and Alfa-Aesar suspensions with particle concentration of 20 wt.-% were not included in the decision to determine the most suitable suspension characteristics, because the laser processing of scratch resistant  $\text{Al}_2\text{O}_3$  layers requires the greatest possible layer thicknesses.

The green Alu-C layers, when viewed with the naked eye, appear as homogenous coatings. Light-microscopy images, however, reveal a tendency to form drying cracks. According to these investigations, drying cracks appear only occasionally at reduced layer thicknesses. For thicker coatings, produced of high solid loaded suspensions, drying cracks extend



throughout the full depth of the layer. The characteristics of the substrate chosen have no effect on how many cracks are generated.

By contrast, the layers produced of AKP-50 and Alfa Aesar powders are crack-free and homogeneous. The surface topographies of these layers produced of 20 wt.-% AKP-50 and Alfa Aesar powders are depicted in the following Figure 23. Suspensions with increased proportions of solids do not significantly impede surface morphology of coatings.

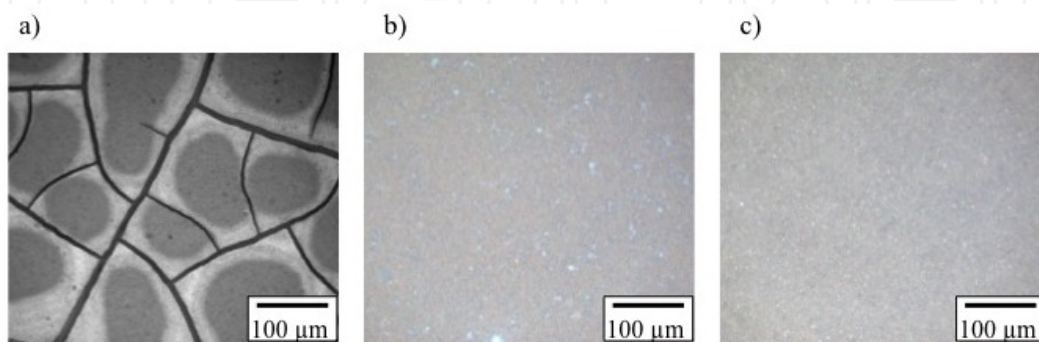


**Figure 23.**  $\text{Al}_2\text{O}_3$  green layers: Alu-C green layers produced of suspensions showing a solid concentration of 20 wt.-% (a), AKP-50 green layers (b) and Alfa Aesar green layers (c) produced of suspensions showing a solid concentration of 20 wt.-%. All green layers shown have been processed onto soda lime glass substrates.

### 5.3. Laser processing of alumina thin films and characterization

The following Figure 24 depicts light optical microscope images of laser processed Alu-C layers. The parameters were not changed with the exception of the scanning speed.

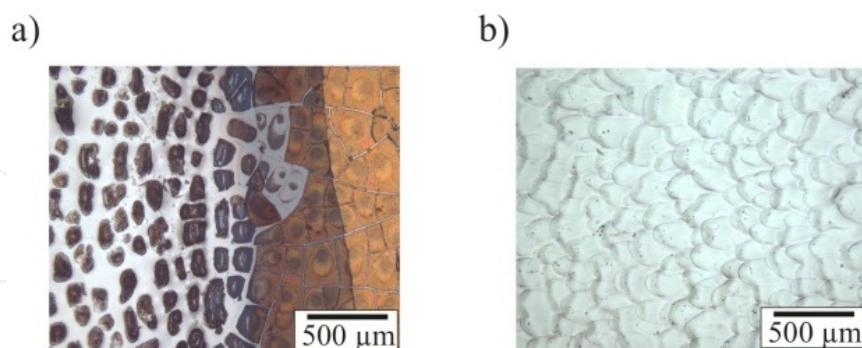


**Figure 24.** Light optical microscope images of Alu-C layers processed by dip-coating and subsequent  $\text{CO}_2$ -laser technique. For the structures shown laser line spacing was 0.1 mm, focused laser beam diameter was 1.0 mm and laser power density was set to  $4000 \text{ W/cm}^2$ . The scanning speed was varied as follows: 400 mm/s (a) and 200 mm/s (b).

Unlike other topographies, the Figure 24a shows an incomplete laser processed layer. Building bridges between laser sintered and green, not sintered areas are clearly visible. This effect is caused by the considerably high scanning speed of 400 mm/s in which the cracks already contained in the green layer were propagated. Simultaneously, the green layered,



floe oriented microstructures resulting in brownish to black discoloration and complete in-transparency. The discoloration of the coating results from incomplete thermal degradation of polymer additives used.

The microstructure of laser processed green layers remains almost unchanged by reducing the scanning speed. The coloration of the floe-oriented microstructure only is varied from dark brown to light brown. A further decrease of the scanning speed down to 300 mm/s finally caused the floe-oriented microstructure to be increased and completely transparent. Singular floe-oriented microstructures are characterized by remaining pin holes and bubbles. From a scanning speed of 250 mm/s and less these heterogeneities disappeared, even though, inbetween singular floe-oriented micro zones not coated areas are observed. This surficial micro-structure is thus termed in the following as “island structure”. Finally, a further increase of the specific laser power density by a further reduction of the scanning speed down to 200 mm/s causes completely densified and transparent coatings. These coatings are characterized by a shed-like external micro-structure. The orientation of the sheds takes place perpendicular to the scanning direction of the laser beam. Consequently the laser scanning lines of the microstructure shown in Figure 24b are run from the top to the bottom.

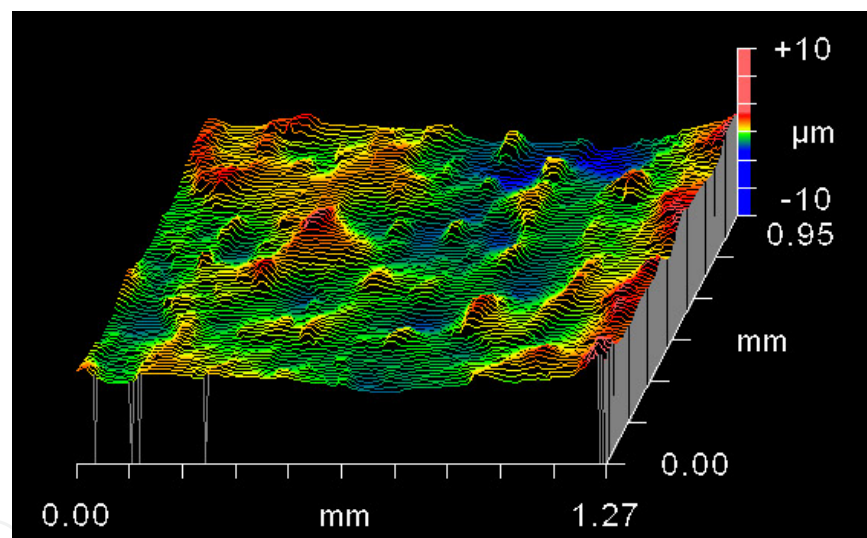


**Figure 25.** Topography of laser scanned alumina coating onto borosilicate substrates analysed by white light interferometry (WLI). Dual laser processing at corresponding scanning direction results in a decreased surface roughness of the irradiated sample

Multiple scanning was performed in order to avoid the formation of the shed-like microstructures and, by that way, to improve the transparency of the as-laser processed layers. The following Figure 25 depicts the sample topography after dual laser scanning moves. The laser powder density used has to be reduced to  $3000 \text{ W/cm}^2$ , in order to restrict the laser energy quantity absorbed by the irradiated surface. The scanning speed was fixed at 200 mm/s, as mentioned before. The smoothed surface of Figure 25 is twofold laser irradiated. In this case first and second laser run are characterized by consistent scanning direction. Here, the mean roughness is in the range of  $0.7 \text{ } \mu\text{m}$ .

In another specific case, the scanning direction of the second laser run has been rotated  $90^\circ$  with respect to the first run. Here, the surface roughness is significantly reduced to  $0.3\ \mu\text{m}$ .

The WLI and SEM analysis show that the thickness of the anti scratch alumina coatings is difficult to determine. Therefore, EDX mappings of breaking edges of the as-laser processed and alumina coated borosilicate samples were captured.

The EDX mappings show that the thickness of the scratch-resistant layer processed by laser irradiation is in the range between  $20\ \mu\text{m}$  and  $40\ \mu\text{m}$ . Moreover, it was found by the analysis results that the coating does not consist of the pure alumina phase, but also a certain Si-concentration in the layer has been assessed.

Consequently, pure alumina green bodies were processed, laser sintered and analysed, in order to investigate the interaction between the laser beam and the coated substrate surface. The following SEM topography shown in Figure 26 depicts a breaking edge of a laser sintered alumina green body with detail magnification. The following Figure 26 shows the edge of a layer processed by high scanning rate of  $350\ \text{mm/s}$  causing surface-near isolated floe-oriented microstructures of alumina. Alumina rich zones, however, are largely free from Si intercalations.

The laser irradiation parameters given in Figure 27 lead to the processing of completely densified alumina coatings. First, the SEM topography shows that the thickness of the coatings obtained varies between  $150\ \mu\text{m}$  and  $200\ \mu\text{m}$ .

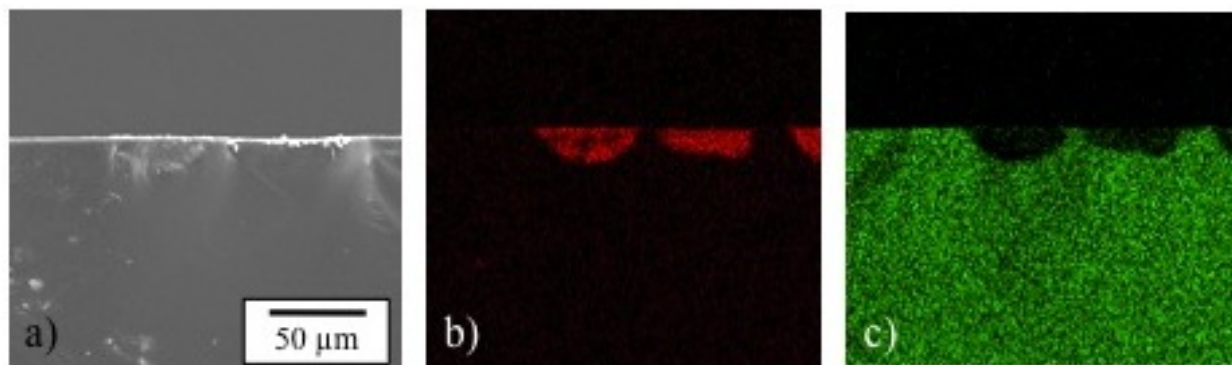


**Figure 26.** SEM topography of front edge Alu-C layer showing near-surface floe-oriented alumina microstructures (a), EDX mapping showing red coloured dots of Al-k- $\alpha$  peaks (b) and EDX mapping showing green coloured dots of Si-k- $\alpha$  peaks (c).

Detail magnification shown in Figure 27a represents a completely densified layer. The transition between completely densified layer and porous residual structure is depicted in detail magnification of Figure 27b.

Even at a distance of  $100\ \mu\text{m}$  below the densified layer the thermal impact of the laser irradiation and absorption of laser energy is observed as it is shown in detail magnification of Figure 26c. Compared to the untreated green structure (see detail magnification of Figure 26d) the grain structure of Figure 26c reveals significant grain growth effect caused by laser energy absorption.

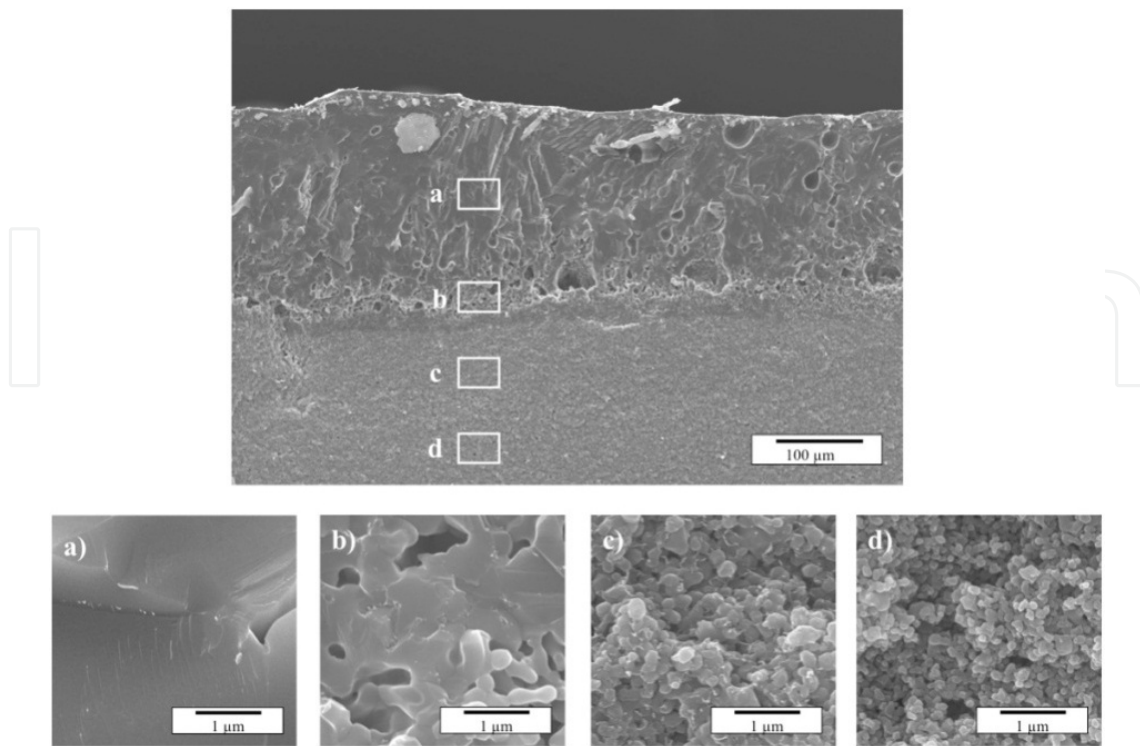


**Figure 27.** SEM topography of a breaking edge of casted alumina green body made of AKP-50 powder after laser irradiation ( $v_{scan} = 200 \text{ mm/s}$ ; laser beam energy density  $4000 \text{ W/cm}^2$ ).

X-ray diffraction (XRD) patterns of a laser irradiated alumina green body and a laser irradiated alumina coating onto borosilicate glass substrate indicate the pure  $\alpha$ -alumina phase. The crystalline state of the green layer is converted to an amorphous structure after laser irradiation as soon as Si atoms diffuse into the alumina phase and significantly high cooling rates are achieved. However, laser sintering of glass substrates coated with alumina layers enables the effective and sustainable processing of scratch resistant protecting layers. Within these application areas, laser processing is expected to develop as a sustainable production methodology. Furthermore, the study showed that laser sintering model systems are difficult to evaluate, because material characteristics and specific absorption behavior of laser energy controls the as-processed coatings substantially.

## 6. Conclusion

Comparative investigations include the processing of dense YSZ electrolyte layers in thicknesses between  $5 \text{ }\mu\text{m}$  and  $20 \text{ }\mu\text{m}$  by means of electrophoretic deposition of aqueous YSZ suspensions and subsequent thermal co-sintering. The resulting micro-tubular NiO-YSZ/YSZ-composite has shown promising potential to be used as SOFC key components.

In this study, it was shown that electrophoretic deposition enables the processing of green, crack-free YSZ thin layers, based on sustainable and simple processing methodologies. The layer thickness, however, was not homogeneous over the entire cross section. Thermal sin-

tering programs used resulted in crack-free co-sintered composites. During sintering investigations, a specific impact of the green in the sintering microstructure was observed: Increased green densities generally result in increased grain growth effects. The two-step-sintering approach enables the complete densification of the sintered YSZ layers at a maximum sintering temperature of 1250 °C. The mean grain size achieved at these conditions is below 1  $\mu\text{m}$ . However, a sintering temperature of 1350 °C is necessary in order to guarantee the electrical conductivity of the NiO-YSZ anode support.

Reducing sintering atmospheres would result in an increase of the anode porosity, independent of the sintering programs used previously. The total porosity after anode reduction to the Ni-YSZ-system consists of the porosity achieved after two-step-sintering and the porosity formed according to the reduction process. Three layered systems composed of micro-tubular Ni-YSZ anode supports, YSZ electrolyte layers and LSM cathodes have already been tested successfully as prototype cells for SOFC applications.

The framework of the efforts to deal with thermal and laser sintering problems of green layer densification include the processing of transparent, scratch-resistant coatings made of alumina and the production of thin electrolyte layers made of YSZ for energy applications.

The processing of transparent scratch-resistant alumina coatings started with the evaluation of suitable suspension conditioning methods. It was shown that in the light of the experiences gained, three different alumina powders were tailored in terms of their suitable aqueous suspension characteristics. These starting materials were used to develop alumina dip coatings on borosilicate glass substrates.

Because of the different powder characteristics, the process development succeeds provided that a careful tailoring of specific suspension characteristics (particle concentration, pH, additive type and concentration, viscosity) is considered.

The different layers derived from the developed suspensions are optimized so that homogeneous and thick green layers are processed.

The results of the laser irradiation experiments showed first that it was not necessary to debind the methylcellulose additive within a subsequent debinding step. Temperatures formed under the influence of laser absorption cause complete degradation and evaporation of polymer additives without any structural change of the coatings. The subsequent laser irradiation experiments showed that reduced laser powder densities result in an incomplete densification of the processed coatings. Once a critical laser power density is achieved (4000 W/cm<sup>2</sup> in this specific case) a complete densification of the coated surface is observed. Optical characteristics of laser-irradiated coatings, above all transparency, have been affected by single laser irradiation processing caused by significant roughness of the surficial coating layers. The subsequent dual laser sintering methodology lead to significantly reduced surface roughness and increased transparency. Based on comparative sintering investigations with casted alumina green bodies, EDX mappings and XRD analysis showed that Si atoms diffuse into the alumina layer during laser densification of the coating. Caused by significantly high cooling rates as-processed and densified oxide Si-Al-layers are generally refer-



red to as amorphous. However, caused by the extended Al atoms within the layer, a increase of strength, toughness and scratch resistance is observed.

## Author details

Guido Falk\*, Katrin Klein and Christoph Rivinius

\*Address all correspondence to: [g.falk@nanotech.uni-saarland.de](mailto:g.falk@nanotech.uni-saarland.de)

Saarland University, Chair Powder Technology of Glass and Ceramics, Saarbruecken, Germany

## References

- [1] Petzold A, Pöschmann H. Email und Emailliertechnik. Stuttgart: Deutscher Verlag f. Grundstoffindustrie; 1992.
- [2] Dietzel AH. Emaillierung. Berlin: Springer-Verlag; 1981.
- [3] Hennicke HW, Padel A. Emaillierungen mit kristallinen Einlagerungen für Einsätze bei hohen Temperaturen (Hochtemperaturemails). Mitteilungen des Vereins Deutscher Emailfachleute e.V. 1991; 39 25-36.
- [4] Sölter H-J, Müller U, Lugscheider E. High-Speed Temperature Measurement for On-Line Proess Control and Quality Assurance during Plasma Spraying. Therm. Spraying 1992; 24 169-175.
- [5] Lugscheider E, Jungklaus H, Wielage B, Henker A. Plasmaspritzen von Titanhartstoffen-Neue Möglichkeiten zum Verschleißschutz. Schweißen & Schneiden 1995; 47 822-831.
- [6] Fehringer G, Janes S, Wildersohn M, Clasen R. Proton-conducting ceramics as electrode/electrolyte-materials for SOFCs: Preparation, mechanical and thermal-mechanical properties of thermal sprayed coatings, material combination and stacks. J. Eur. Ceram. Soc. 2004; 24 705-715.
- [7] Dubourg L, Lima RS, Moreau C. Properties of alumina-titania coatings prepared by laser-assisted air plasma spraying. Surf. Coat. Technol. 2007; 201 6278-6284.
- [8] Lutz EH. Microstructure and Properties of Plasma Ceramics. J. Am. Ceram. Soc. 1994; 77 1274-1280.
- [9] Bennett MJ, Knights CF, Ayres CF, Tuson AT, Desport JA, Rickerby DS, Saunders SRJ, Coley KS. Corrosion-resistant silica coatings obtained by plasma-assisted chemical vapour deposition. Mater. Sci. Eng. 1991; A139 91-102.



- [10] He JL, Chu CH, Wang HL, Hon MH. Corrosion protection by PECVD-SiO<sub>x</sub> as a top coating on TiN-coated steel. *Surf. & Coatings Technol.* 1994; 63 15-23.
- [11] Lee J-S, Liu K-S, Lin I-N. Deposition of diamond films on SiO<sub>2</sub> surfaces using a high power microwave enhanced chemical vapor deposition process. *J. Appl. Phys.* 1997; 81 486-491.
- [12] Menzler NH, Tietz F, Uhlenbruck S, Buchkremer HP, Stöver D. Materials and manufacturing technologies for solid oxide fuel cells. *J. Mater. Sci.* 2010; 45 3109-3135.
- [13] Tietz F, Buchkremer H-P, Stöver D. 10 Years of Materials Research for Solid Oxide Fuel Cells at Forschungszentrum Jülich. *J. Electroceram.* 2006; 17 701-707.
- [14] Pal UB, Singhal SC. Electrochemical Vapor Deposition of Yttria-stabilized Zirconia Films. *J. Electrochem. Soc.* 1990; 137 2937-2941.
- [15] Haart LGJd. 26. IFF-Ferienkurs in Jülich: Elektrokeram. Materialien, Grundlagen und Anwendungen.: conference proceedings, 1995.
- [16] Steinberger-Wilckens R, Blum L, Buchkremer H-P, Gross S, Haart LBd, Hilpert K, Nabielek H, Quadackers WJ, Reisgen U, Steinbrech RW, Tietz F. Overview of the development of solid oxide fuel cells at Forschungszentrum Juelich. *Int. J. Appl. Ceram. Technol.* 2006; 3 470-476.
- [17] Honegger K, Engler J. PVD and Thermal Spray Deposition of electrolyte/electrode system. *Jahresbericht 1999. Sulzuer HEXIS AG; 1999*
- [18] Henne R, Fendler E, Lang M. 1. European SOFC Forum: conference proceedings, Luzern/Ch. 1994.
- [19] Friis M, Persson C, Wigren J. Influence of particle in-flight characteristics on the microstructure of atmospheric plasma sprayed yttria stabilized ZrO<sub>2</sub>. *Surf. Coat. Technol.* 2001; 141 115-127.
- [20] Zhao B, Zhang R, Lu L, Xie H. Preparation of La<sub>x</sub>Sr<sub>1-x</sub>MnO<sub>3</sub> ultrafine powder by spray pyrolysis. *Mater. Sci. & Eng.* 1997; B49 36-41.
- [21] Maric R, Ohara S, Fukui T, Inagaki T, Fujita J. High-performance Ni-SDC cermet anode for solid oxide fuel cells at medium operating temperature. *Electrochem. Solid State Lett.* 1998; 1 201-203.
- [22] Jansen H, Buchkremer HP, Stöver D, Wippermann K. Third international Symposium of Solid Oxide Fuel Cells: conference proceedings, Honolulu. *Electrochemical Society; 1993.*
- [23] Wilkenhöner R, Hauber T, Malléner W, Stöver D. Herstellung von elektroaktiven Schichten für die Hochtemperatur-Brennstoffzelle mittels Wet Powder Spraying. *Fortschrittsber. Dtsch. Keram. Ges.* 1995; 10 263-269.
- [24] Schüller E, Vaßen R, Stöver D. Thin Electrolyte Layers for SOFC via Wet Powder Spraying (WPS). *Adv. Eng. Mat.* 2002; 4 659-662.

- [25] Mayen-Mondragon R, Falk G, Clasen R. Electrophoretic Impregnation/Deposition Complemented with Polymeric Templating for the Fabrication of Functionalized-Porosity Layered- Ceramics: A Solid-Oxide-Fuel-Cells Approach. *J. Am Ceram. Soc.* 2011; 95 593-599.
- [26] Cherng JS, Sau JR, Chung CC. Aqueous electrophoretic deposition of YSZ electrolyte layers for solid oxide fuel cells. *J. Solid State Electrochem.* 2008; 12 925-933.
- [27] Hosomi T, Matsuda M, Miyake M. Electrophoretic deposition for fabrication of YSZ electrolyte film on non-conducting porous NiO-YSZ composite substrate for intermediate temperature SOFC. *J. Eur. Ceram. Soc.* 2007; 27 173-178.
- [28] Falk G, Böhm N, Delaporte P-G, Clasen R. 31st International Conference on Advanced Ceramics and Composites: conference proceedings, Daytona Beach American Ceramic Society; 2007.
- [29] Boccaccini AR, Roether JA, Thomas BJC, Shaffer MS, Chavez E, Stoll E, Minay EJ. The electrophoretic deposition of inorganic nanoscaled materials - a review. *J. Ceram. Soc. Japan* 2006; 114 1-14.
- [30] Neirinck B, Fransaer J, Biest OVd, Vleugels J. Aqueous electrophoretic deposition in asymmetric AC electric fields (AC-EPD). *Electrochem. Commun.* 2009; 11 57-60.
- [31] Bordia RK, Raj R. Sintering behavior of ceramic films constrained by a rigid substrate. *J. Am. Ceram. Soc.* 1985; 68 287-292.
- [32] Bordia RK, Scherer GW. On constrained sintering - III. rigid inclusions. *Acta metall.* 1988; 36 2411-2416.
- [33] Scherer GW, Garino T. Viscous sintering on a rigid substrate. *J. Am. Ceram. Soc.* 1985; 68 216-220.
- [34] Jagota A, Mikeska KR, Bordia RK. Isotropic constitutive model for sintering particle packings. *J. Am. Ceram. Soc.* 1990; 73 2266-2273.
- [35] Jagota A. Simulation of the Viscous Sintering of Coated Particles. *J. Am. Ceram. Soc.* 1994; 77 2237-2239.
- [36] Jagota A, Scherer GW. Viscosities and Sintering Rates of Composite Packings of Spheres. *J. Am. Ceram. Soc.* 1995; 78 521-528.
- [37] Wakai F, Aldinger F. Equilibrium configuration of particles in sintering under constraint. *Acta Mater.* 2003; 51 641-652.
- [38] Wakai F, Brakke KA. Mechanics of sintering for coupled grain boundary and surface diffusion. *Acta Mater.* 2011; 59 5379-5387.
- [39] Bordère S, Gendron D, Bernard D. Improvement in the accuracy of calculated interface morphologies within Monte Carlo simulations of sintering processes. *Scripta Mater.* 2006; 55 267-270.

- [40] Zhao Y, Dharani LR. Theoretical model for the analysis of a ceramic thin film sintering on a non-sintering substrate. *Thin Solid Films* 1994; 245 109-114.
- [41] Olevsky EA, Tikare V, Garrino T. Multi-scale study of sintering: A review. *J. Am. Ceram. Soc.* 2006; 89 1914-1922.
- [42] Tzeng S-Y, Jean J-H. Stress development during constrained sintering of alumina/glass/alumina sandwich structure. *J. Am. Ceram. Soc.* 2002; 85 335-340.
- [43] Mohanram A, Lee S-H, Messing GL, Green DJ. Constrained sintering of low temperature co-fired ceramics. *J. Am. Ceram. Soc.* 2006; 89 1923-1929.
- [44] Amin Z, Dalgarno KW, Comyn TP, Tavernor AW. Metal-electroceramic bonding in PZT through the selective application of laser energy. *J. Mat. Sci* 2006; 41 2831-2838.
- [45] X. Wang, P. Xiao, M. Schmidt, Li L. Laser processing of yttria stabilized zirconia/alumina coatings on FeCrAlloy substrates. *Surface & Coatings Technol.* 2004; 187 370-376.
- [46] Exner H, Reinecke AM, Nieher M. Laser beam sintering of thin alumina coatings on metals. *J. Ceram. Proc. Res.* 2002; 3 66-69.
- [47] Kurella A, Dahorte NB. Laser induced multi-scale textured zirconia coating on Ti-6Al-4V. *J. Mater. Sci.: Mater. Med.* 2006; 17 565-572.
- [48] Sarkar P, De D, Rho H. Synthesis and microstructural manipulation of ceramics by electrophoretic deposition. *J. Mater. Sci.* 2004; 39 819-823.
- [49] Harbach F, Nienburg H. Homogeneous Functional Ceramic Components through Electrophoretic Deposition from Stable Colloidal Suspensions - I Basic Concepts and Application to Zirconia. *J. Eur. Ceram. Soc.* 1998; 18 675-683.
- [50] Wittwer H, Krüger HG. Möglichkeiten und Grenzen der Elektrophorese. *cfi/Ber. DKG* 1995; 72 556-560.
- [51] Fehringer G. Herstellung von Schichten aus Nanopulvern über das Dip-Coating Verfahren mit wässrigen Suspensionen, über atmosphärisches Plasmaspritzen und Elektroschmelzsprühen. Dissertation. Universität des Saarlandes Saarbrücken; 2008.